

High Energy Observations of XRF 030723: Evidence for an Off-axis Gamma-Ray Burst?

N. R. Butler¹, T. Sakamoto^{3,4}, M. Suzuki³, N. Kawai^{3,4}, D. Q. Lamb², C. Graziani², T. Q. Donaghy², A. Dullighan¹, R. Vanderspek¹, G. B. Crew¹, P. Ford¹, G. Ricker¹, J-L. Atteia⁶, A. Yoshida^{4,7}, Y. Shirasaki⁸, T. Tamagawa⁴, K. Torii¹⁷, M. Matsuoka⁹, E. E. Fenimore⁵, M. Galassi⁵, J. Doty¹, J. Villasenor¹, G. Prigozhin¹, J. G. Jernigan¹⁰, C. Barraud⁶, M. Boer¹¹, J-P. Dezalay¹¹, J-F. Olive¹¹, K. Hurley¹⁰, A. Levine¹, F. Martel¹, E. Morgan¹, S. E. Woosley¹², T. Cline¹³, J. Braga¹⁴, R. Manchanda¹⁵, and G. Pizzichini¹⁶

¹Center for Space Research, Massachusetts Institute of Technology, 70 Vassar Street, Cambridge, MA, 02139

²Department of Astronomy and Astrophysics, University of Chicago, IL, 60637

³Department of Physics, Tokyo Institute of Technology, 2-12-1 Ookayama, Meguro-ku, Tokyo 152-8551, Japan

⁴RIKEN (Institute of Physical and Chemical Research), 2-1 Hirosawa, Wako, Saitama 351-0198, Japan

⁵Los Alamos National Laboratory, P.O. Box 1663, Los Alamos, NM, 87545

⁶Laboratoire d'Astrophysique, Observatoire Midi-Pyrénées, 14 Ave. E. Belin, 31400 Toulouse, France

⁷Department of Physics, Aoyama Gakuin University, Chitosedai 6-16-1, Setagaya-ku, Tokyo 157-8572, Japan

⁸National Astronomical Observatory, Osawa 2-21-1, Mitaka, Tokyo 181-8588, Japan

⁹Tsukuba Space Center, National Space Development Agency of Japan, Tsukuba, Ibaraki, 305-8505, Japan

¹⁰University of California at Berkeley, Space Sciences Laboratory, Berkeley, CA, 94720-7450

¹¹Centre d'Etude Spatiale des Rayonnements, CNRS/UPS, B.P.4346, 31028 Toulouse Cedex 4, France

¹²Department of Astronomy and Astrophysics, University of California at Santa Cruz, 477 Clark Kerr Hall, Santa Cruz, CA 95064

¹³NASA Goddard Space Flight Center, Greenbelt, MD, 20771

¹⁴Instituto Nacional de Pesquisas Espaciais, Avenida Dos Astronautas 1758, Saõ José dos Campos 12227-010, Brazil

¹⁵Department of Astronomy and Astrophysics, Tata Institute of Fundamental Research, Homi Bhabha Road, Mumbai, 400 005, India

¹⁶Consiglio Nazionale delle Ricerche (IASF), via Piero Gobetti, 101-40129 Bologna, Italy

¹⁷Department of Earth and Space Science, Graduate School of Science, Osaka University 1-1 Machikaneyama-cho, Toyonaka, Osaka 560-0043, Japan

ABSTRACT

We report *High Energy Transient Explorer 2 (HETE-2)* Wide Field X-ray Monitor/French Gamma Telescope observations of XRF 030723 along with observations of the XRF afterglow made using the 6.5m Magellan Clay telescope and the *Chandra X-ray Observatory*. The observed peak energy $E_{\text{pk}}^{\text{obs}}$ of the νF_{ν} burst spectrum is found to lie within (or below) the WXM 2-25 keV passband at 98.5% confidence, and no counts are detected above 30 keV. Our best fit value is $E_{\text{pk}}^{\text{obs}} = 8.4_{-3.4}^{+3.5}$ keV. The ratio of X-ray to γ -ray flux for the burst follows a correlation found for GRBs observed with *HETE-2*, and the duration of the burst is similar to that typical of long-duration GRBs. If we require that the burst isotropic equivalent energy E_{iso} and E_{pk} satisfy the relation discovered by Amati et al. (2002), a redshift of $z = 0.38_{-0.18}^{+0.36}$ can be determined, in agreement with constraints determined from optical observations. We are able to fit the X-ray afterglow spectrum and to measure its temporal fade. Although the best-fit fade is shallower than the concurrent fade in the optical, the spectral similarity between the two bands indicates that the X-ray fade may actually trace the optical fade. If this is the case, the late time rebrightening observed in the optical cannot be due to a supernova bump. We interpret the prompt and afterglow X-ray emission as arising from a jetted GRB observed off-axis and possibly viewed through a complex circumburst medium due to a progenitor wind.

Subject headings: gamma rays: bursts — supernovae: general — X-rays: general

1. Introduction

Approximately 1/3 of all bursts detected by the *HETE-2* satellite, excluding X-ray bursts and bursts due to known Galactic sources, have fluences in the X-rays (2-30 keV) which are larger than those measured in the γ -rays (30-400 keV). These are the “X-ray Flashes” (XRFs) (Heise et al. 2000). A similar fraction of XRFs to γ -ray Bursts (GRBs) was observed by *GINGA* (Strohmayer et al. 1998), while *BATSE* lacked the low energy response to detect so large a fraction of XRFs relative to GRBs. Nonetheless, for bursts detected by both *BATSE* and *BeppoSAX*, it appears that XRFs can be described by Band et al. (1993) models with parameters consistent with those found for GRBs, except with lower fluxes and νF_{ν} peak energies ~ 10 – 100 times smaller (Kippen et al. 2002).

Sakamoto et al. (2003) have demonstrated additional links between XRFs and GRBs by showing that the prompt emission from XRF 020903, the first XRF with an established

redshift (Soderberg et al. 2004a), satisfies and extends two correlations observed for GRBs. First, the burst satisfies the relation found by Barraud et al. (2003) between 7-30 keV and 30-400 keV fluences in bursts observed by the *HETE-2* French Gamma Telescope (FREGATE). Second, the isotropic-equivalent energy E_{iso} tracks the νF_{ν} spectral peak energy E_{pk} as found for GRBs by Amati et al. (2002), extending the correlation by a factor ~ 300 .

Much theoretical (and observational) energy has focused recently on XRFs, driven by the strong possibility that XRFs represent an extension of the GRB population to softer energies. Models are focused primarily on differences in the jet physics (see Zhang & Mészáros (2002) for an overview). The data for XRF 030723, and the well-sampled data from its optical and X-ray afterglows, are excellent discriminators for these models, as we discuss in Sections 3, 4, and 5.

2. Prompt Observations

2.1. Localization

XRF 030723 was detected by the *HETE-2* FREGATE, WXM (Wide Field X-ray Monitor), and SXC (Soft X-ray Camera) instruments at 6:28:59 UT on 2003 July 23 (Prigozhin et al. 2003). A GCN burst alert was issued 42s later, reporting a flight-derived WXM localization with a 30 arcmin radius (90% confidence). Ground analysis of the WXM data produced a refined 9.4 arcmin error radius localization that was reported in a GCN Notice at 09:47:25 UT. It is centered at R.A. = $21^{\text{h}}48^{\text{m}}52^{\text{s}}$, decl. = $-27^{\circ}41'16''$ (J2000.0). Ground analysis of the SXC data provided an initial localization that was disseminated as a GCN Notice at 13:38:19 UT. A refined 2 arcmin radius error circle centered at R.A. = $21^{\text{h}}49^{\text{m}}27.4^{\text{s}}$, decl. = $-27^{\circ}42'01''$ (J2000.0) was reported by Prigozhin et al. (2003). These error regions are shown in Figure 1.

In our analysis of the XRF 030723 prompt emission, we apply a “cut” to the WXM time- and energy-tagged data (TAG data), using only the photons from the pixels on the five wires in the X-detector (XA0, XA1, XA2, XB0, XB1) and the three wires in the Y-detector (YA0, YA1, YA2) that were illuminated by the burst. This entails including only the photons from the portions of each wire which would be illuminated by an X-ray source located at the position of the optical transient (OT) reported by Fox et al. (2003) (Section 3).

2.2. Temporal Properties

Figure 2 displays the WXM and FREGATE light curves for XRF 030723 in four energy bands. A linear fit to the 30-400 keV data (4th panel, Figure 2) shows that there are few, if any, net counts above 30 keV. The burst temporal profile below 25 keV is consistent with the presence of a single peak, and the burst durations in this band do not appear to depend strongly on energy. Table 1 gives t_{90} and t_{50} durations for the burst in the 2-5, 5-10, 10-25, and 2-25 keV bands.

2.3. Spectrum

The WXM detector response matrix has been well-calibrated using observations of the Crab nebula (Shirasaki et al. 2002). In the spectral fits, we include only the photons that registered on the five wires in the X-detectors and the three wires in the Y-detectors that were illuminated by the burst, as mentioned above. Since the variation in the gain is not uniform at the ends of the wires in the WXM detectors (Shirasaki et al. 2000), we use only the photon counts that registered in the central ± 50 mm region of the wires to construct the spectra of the burst. We include all of the photons that register in the central regions of these wires (i.e, we use the full 2-25 keV energy range of the WXM). We analyze the summed data from the eight wires, taking the normalizations on all wires to be the same. The FREGATE spectral response has been verified with observations of the Crab nebula as described in Barraud et al. (2003). We consider the WXM data in the 2-25 keV band and the FREGATE data in the 7-100 keV band, and we do not rebin the pulse height channels. We carry out a set of fits for the burst from -1.25s to 30s from the trigger time (see the dotted lines in Figure 2), that include the spectral data from both the WXM and the FREGATE. Background data are taken from the time intervals -37.2s to -14.9s and 44.2s to 99.4s, relative to the trigger time. We use the XSPEC v11.2.0 software package to do the spectral fits. All errors refer to the 90% confidence regions, unless otherwise noted.

Table 2 presents the results of our time-averaged spectral analysis for XRF 030723. The data are well fitted by a power-law model (Figure 3) and considerably less well-fitted by a blackbody model. The data bins above 30 keV do not affect the blackbody fit. In the 2-30 keV band, the fit yields $\chi^2_\nu = 1.484$ for 50 degrees of freedom. Thus, it is rejectable at 98.5% confidence.

Band models can be used to describe the spectra of essentially all GRBs. The high-energy photon index of a Band model must satisfy $\beta < -2$ in order for the νF_ν spectral peak energy to lie in or below our passband. The index in the best fit power-law model is

consistent with $\beta < -2$. If we exclude the counts below 10 keV, retaining 66 of 84 data bins, the best-fit power-law index (-3.2) is less than -2 at 98.5% confidence (likelihood ratio test: $\Delta\chi^2 = 5.93$ for 1 additional degree of freedom). This is the confidence at which we claim the burst to be an XRF. If the νF_ν peak energy of the burst were not established in this fashion to lie in or below the WXM band (2-25 keV), the burst could potentially be a faint GRB, with $E_{\text{pk}}^{\text{obs}} > 100$ keV.

A proper determination of $E_{\text{pk}}^{\text{obs}}$ should be found using a Band model. The parameters of our best fit models are shown in Table 2. The 90% confidence parameter regions are not well defined for the Band models; so we quote the 68% confidence regions in Table 2 instead. If we assume $\beta < -2$, as argued above, we can generate firm limits on $E_{\text{pk}}^{\text{obs}}$ using the “constrained” Band model formalism developed by Sakamoto et al. (2003). This model assumes $\beta < -2$ and allows the Band model to produce a pure power-law only with the high energy index. We find $E_{\text{pk}}^{\text{obs}} = 8.4_{-3.4}^{+3.5}$ keV. The posterior probability distribution for $E_{\text{pk}}^{\text{obs}}$, along with the locations of this 90% confidence interval and the $3\text{-}\sigma$ upper limit of 15.0 keV, are plotted in Figure 4. We find consistent values for $E_{\text{pk}}^{\text{obs}}$ using cutoff power-law model and Band model fit with $\alpha = -1$. This is a typical α value for GRBs, and it allows for excellent fits to the XRF 030723 data.

Table 3 displays fluences and peak fluxes determined from fits of the cutoff power-law model in various energy bands. The power-law model produces a lower value for the 30-400 keV flux than does the cutoff power-law model. Applying the best-fit power-law model in Table 2, the burst fluence in the 2-30 keV band is $S_X(2 - 30\text{keV}) = 2.9 \pm 0.4 \times 10^{-7}$ erg cm^{-2} , and the burst fluence in the 30-400 keV band is $S_\gamma(30 - 400\text{keV}) = 2.8_{-1.3}^{+1.5} \times 10^{-7}$ erg cm^{-2} . For both the cutoff power-law model and the power-law model we have $\log[S_X(2 - 30\text{keV})/S_\gamma(30 - 400\text{keV})] > 0$, which is our operating definition of an XRF.

Finally, we test for possible spectral evolution during the burst by fitting the WXM and FREGATE data divided into two time portions. We take data from the first half of the burst (from -1.25s to 15s) and from the second half of the burst (from 15s to 30s), and we fit both portions using a power-law model in the same fashion as we fit the full data set above. A power-law fit to the first data half yields $\beta_1 = -1.9_{-0.1}^{+0.2}$, with $\chi_\nu^2 = 72.95/82$. For the second half of the data, we find $\beta_2 = -2.9_{-1.4}^{+0.8}$, with $\chi_\nu^2 = 71.77/82$. Fitting both halves jointly and allowing one common spectral index, we find $\beta = \beta_1 = \beta_2 = -1.9_{-0.2}^{+0.1}$, with $\chi_\nu^2 = 150.3/165$. Hence, there is evidence for a hard-to-soft spectral evolution during the burst at 98.2% confidence ($\Delta\chi^2 = 5.58$ for 1 additional degree of freedom). Hard-to-soft evolution is common in GRBs, and it was reported by Sakamoto et al. (2003) at similar confidence for XRF 020903.

3. Optical Afterglow Observations

The refined error regions are shown in Figure 1, enclosing the location of a fading OT detected by Fox et al. (2003). The quoted position of the OT is R.A. = $21^h49^m24.40^s$, decl. = $-27^\circ42'47.4''$ (J2000.0), with an uncertainty of less than $0.5''$ in either dimension. Using the 60-inch telescope at Mount Palomar, Fox et al. (2003) observed the source to fade by 1.1 mag, $R \sim 21.3$ 1.23 days after the GRB to $R \sim 22.4$ 2.23 days after the GRB. This source, likely the optical afterglow associated with the GRB, was also detected by Fox et al. (2003) in the Ks-band ($Ks \sim 18.65$) with the Hale 200-inch telescope at Mount Palomar 1.23 days after the burst, however the source was below the detection threshold ($Ks \sim 19.0$) at 2.23 days.

From 24.8 hours to 25.2 hours after the burst (centered on July 24.31 UT), we observed the SXC error circle with the LDSS2 instrument on the 6.5m Magellan Clay telescope at Las Campanas Observatory in Chile. Four 6-minute R-band exposures were taken in $\sim 0.6''$ seeing. Our photometry has been calibrated against the USNO photometry data reported by Henden (2003). Coaddition of the images gives a limiting magnitude of $R = 24.5$. We detected the source of Fox et al. (2003) with $R = 21.13 \pm 0.05$ (Dullighan et al. 2003a). On July 28.385 UT, 5.13 days after the burst, we again observed the SXC error circle with Magellan. We obtained two 200-second exposures with the MagIC instrument in $\sim 0.8''$ seeing, reaching a limiting magnitude of $R = 24.3$. In the second observation the OT magnitude was $R = 24.2 \pm 0.3$. Including the other detections reported over the GCN (see Figure 7), we estimate a late time power-law decay index of $\alpha = -1.84 \pm 0.04$, and an early power-law decay of $\alpha = -0.8 \pm 0.2$. A break in the light curve can then be inferred to occur at ~ 1.5 days after the burst (see also, Fynbo et al. 2004a). The simple two component power-law picture is, however, inadequate to explain the early faintness (at $t \lesssim 0.5$ days) and the late time rebrightening in the optical afterglow.

Rykoff et al. (2002) argue that the early faintness in the optical afterglow (relative to the afterglow after ~ 1 day) may be due to absorption by material arising from a progenitor wind. However, their measurements (left-most two optical points in Figure 7) are of low significance, and they indicate an early-time flux *higher* than that implied by the observations reported by Fynbo et al. (2004a) (next two optical data points in Figure 7). Fynbo et al. (2004a) suggest a complicated off-axis jet scenario that could possibly explain all four data points.

Fynbo et al. (2004a) (see also, Fynbo et al. 2004b; Tominaga et al. 2004) observed a rebrightening in the R-band optical afterglow at $t \gtrsim t_{\text{GRB}} + 9$ days. Those authors argue that this is due to emission from an underlying supernova component, and the magnitude of the rebrightening implies that the supernova is nearby ($z \sim 0.6$). Dado, Dar, & De Rujula

(2003) also argue in favor of this supernova component interpretation. Alternatively, Huang et al. (2004), and also Liang & Dai (2004), argue that the rebrightening is due to a two component jet as put forward by Berger et al. (2003) for GRB 030329. Regardless of how the rebrightening is interpreted, a low redshift would be consistent with the blue, apparently featureless VLT spectrum observed by Fynbo et al. (2004a), where the lack of Ly- α forest lines implies $z < 2.3$.

Fynbo et al. (2004a) detected a faint ($R = 26.8 \pm 0.4$) galaxy spatially coincident with the optical afterglow using the FORS1 optical camera on the ESO VLT on September 24 UT. From September 29 UT to October 3 UT, Kawai et al. (2003) observed the probable host galaxy with the Subaru Prime Focus Camera on the Subaru telescope and detected the source in the Rc ($Rc = 27.6 \pm 0.4$), Ic, and z' bands.

The source was not detected in the radio. Soderberg, Berger, & Frail (2003) report a $3\text{-}\sigma$ upper limit of $180 \mu\text{Jy}$ at 8.46 GHz for July 26.42 UT.

4. X-ray Afterglow Observations

4.1. Chandra Detection

On 25 July 2003, the *Chandra Observatory* targeted the field of XRF 030723 for a 25 ksec (E1) observation spanning the interval 09:52-17:05 UT on 25 July, 51.4 - 59.0 hours after the burst. The SXC error circle from Prigozhin et al. (2003) was completely contained within the field-of-view of the *Chandra* ACIS-I array. On 4 August 2003, *Chandra* re-targeted the field of XRF 030723 for an 85 ksec followup (E2) observation, spanning the interval 4 August 22:22 UT to 5 August 22:27 UT, 12.69 to 13.67 days after the burst. For this observation, the SXC error circle from Prigozhin et al. (2003) was completely contained within the field-of-view of the *Chandra* ACIS-S3 chip.

As reported in Butler et al. (2003a), 3 candidate point sources were detected within the revised SXC error region in our E1 observation (Figure 5). Positions and other data for these sources are shown in Table 4. None of the sources were anomalously bright relative to objects in *Chandra* deep field observations (see, e.g., Rosati et al. 2002). The brightest object within the SXC error circle (source #1), lies $62''$ from the center of the SXC error circle, and is within $0.7''$ of the optical transient reported by Fox et al. (2003).

Table 4 shows the number of counts detected in E1 and in E2. The E2 observations were reported in Butler et al. (2003b). Accounting for the difference in exposure times and sensitivity, the number of counts detected for a steady source in E2 should be ~ 6 times

the number of counts detected in E1. This factor is greater than the ratio of exposure times, because the ACIS-S3 chip is more sensitive than the ACIS-I chips. (We estimate the additional sensitivity by assuming a power-law spectrum with photon index $\Gamma = -2$ and Galactic absorption.) Thus, sources 3 and 4 appear to have remained constant, while source 1 has faded. The number of counts detected in E2 corresponds to a $\sim 7\sigma$ significance decrease (i.e. factor of 6) in flux since the E1 observation.

4.2. X-ray Afterglow Spectrum and Fade

To properly determine the fade factor for the X-ray afterglow, we fit the E1 and E2 spectral data jointly. We reduce the spectral data using the standard CIAO¹⁸ processing tools. We use “contamarf”¹⁹ to correct for the quantum efficiency degradation due to contamination in the ACIS chips, important for energies below ~ 1 keV. We bin the data into 12 bins, each containing 12 or more counts, and we fit an absorbed power-law model by minimizing χ^2 . The model has three parameters: two normalizations, and one photon index Γ . The absorbing column has been fixed at the Galactic value in the source direction, $N_H = 2.4 \times 10^{20} \text{ cm}^{-2}$ (Dickey & Lockman 1990). The model fits the data well ($\chi^2_\nu = 8.9/9$, Figure 6). The best fit photon number index is $\Gamma = -1.9^{+0.2}_{-0.3}$, which is a typical value for the X-ray afterglows of long duration GRBs (Costa et al. 1999). Using this model, we find that the E1 flux is $2.2 \pm 0.3 \times 10^{-14} \text{ erg cm}^{-2} \text{ s}^{-1}$ (0.5-8.0 keV band), while the E2 flux is $3.5 \pm 0.5 \times 10^{-15} \text{ erg cm}^{-2} \text{ s}^{-1}$ (0.5-8.0 keV band). The decrease in flux between the two epochs can be described by a power-law with a decay index of $\alpha = -1.0 \pm 0.1$. This value of α is consistent with the early power-law decline in the optical (Section 3 for $t \lesssim 1.5$ days after the GRB; however, the index is considerably flatter than the index at $t > 1.5$ days. This flatter X-ray decay may possibly be related to the rebrightening of the optical afterglow reported by Fynbo et al. (2004a). The optical afterglow, had it been observed during our two *Chandra* epochs only, would indicate a fade with $\alpha \sim -1$ (see Figure 7).

¹⁸<http://cxc.harvard.edu/ciao/>

¹⁹http://space.mit.edu/CXC/analysis/ACIS_Contam/script.htm 1

5. Discussion

5.1. Source Properties

The WXM/FREGATE spectrum for XRF 030723 is poorly fit by a blackbody model. Even though the best fit model had a temperature similar to that commonly found in Type I X-ray burst sources (see, e.g., Lewin, van Paradijs & Taam 1993), an association with an X-ray burster can be rejected due to the source’s high Galactic latitude ($b = -49.8^\circ$). No known X-ray burster or globular cluster is coincident with the position of the afterglow and its probable host galaxy. On the contrary, the burst and afterglow energetics and fade properties are similar to those common in GRBs and XRFs, as we now discuss.

Barraud et al. (2003) find a strong correlation between the fluence in the 7-30 keV versus the fluence in the 30-400 keV band for 32 GRBs observed with HETE FREGATE. Sakamoto et al. (2003) find that XRF 020903 supports an extension of the correlation to XRFs. The correlation is described as $S_X(7 - 30\text{keV}) = 3.2_{-1.5}^{+2.7} \times 10^{-3} S_\gamma(30 - 400\text{keV})^{0.643 \pm 0.046}$. For the value of S_γ we find for XRF 030723 from the power-law model, this yields the expectation that $S_X = 2.0_{-0.6}^{+0.4} \times 10^{-7} \text{ erg cm}^{-2}$. This is consistent with the observed value $S_X = 1.6_{-0.4}^{+0.3} \times 10^{-7} \text{ erg cm}^{-2}$. However, for the value of S_γ we find from the cutoff power-law model (which provides a better fit to the XRF 030723 WXM/FREGATE data than does the power-law model) the Barraud et al. (2003) correlation yields the expectation that $S_X = 3.0_{-1.4}^{+2.0} \times 10^{-8} \text{ erg cm}^{-2}$. This flux is a smaller than, and marginally inconsistent with, the observed value $S_X = 1.6 \pm 0.5 \times 10^{-7} \text{ erg cm}^{-2}$. In any case, XRF 030723 has a value for S_X/S_γ near the dividing line between XRFs and “X-ray Rich” GRBs ($S_X/S_\gamma = 1$), and it is likely an important “bridge” event between few keV XRFs like XRF 020903 and classical GRBs and X-ray Rich GRBs.

Sakamoto et al. (2003) find that XRF 020903 supports an extension of the Amati et al. (2002) correlation to XRFs. Although no redshift has been measured for XRF 030723, we have a constraint from the optical that $z < 2.3$ (see Section 3) and possible indications from a rebrightening in the optical that the redshift may be lower yet. The redshift is likely not much lower than $z = 0.5$ due to the faintness of the host galaxy (Fynbo et al. 2004a). In Figure 8, we plot the trajectory of XRF 030723 with redshift, determined from fits of the cutoff power-law model, through the $E_{\text{pk}}-E_{\text{iso}}$ plane. For the range of redshifts which agree with the optical constraints, the *HETE-2* XRF 030723 data also support an extension of the Amati et al. (2002) relation to XRFs. Taking this evidence as proof that XRF 030723 also satisfies the Amati et al. (2002) relation, we can turn the problem around and use the Amati et al. (2002) relation as prior information in our spectral fitting. This makes it possible to derive the best-fit redshift and 90% confidence interval: $z = 0.38_{-0.18}^{+0.36}$. We also derive $E_{\text{iso}} = 2.1_{-1.6}^{+8.7} \times 10^{50}$

erg, and $E_{\text{pk}} = 12.9_{-4.4}^{+7.8}$ keV. We assume a lognormal distribution with standard deviation 0.3 for the intrinsic scatter in the Amati et al. (2002) relation. We assume a cosmology with $(h, \Omega_m, \Omega_\Lambda) = (0.65, 0.3, 0.7)$. Furthermore, we can motivate $z \lesssim 1.0$, using only the XRF data in the observer frame: we find $\hat{z} = 0.59$ for the Atteia (2003) redshift indicator. Use of the redshift indicator \hat{z} is justified in Atteia (2003) via a correlation observed for 17 GRBs detected by *HETE-2* and *BeppoSAX*.

The conclusion that XRF 030723 satisfies the Amati et al. (2002) relation is most strongly dependent upon our determination at 98.5% confidence in Section 2.3 that the $E_{\text{pk}}^{\text{obs}}$ of the burst is well below 100 keV. If this is not the case, then XRF 030723 may actually be a sub-energetic GRB like GRBs 980425 and 031203 (see, Soderber et al. 2004b; Woosley 2004). These bursts apparently do not lie on the Amati et al. (2004) correlation. In the discussion below, we assume that XRF 030723 does satisfy the Amati et al. (2004) relation.

5.2. Testing the Off-axis Jet Model

The prompt spectrum for XRF 030723 is likely not that of a typical GRB, which has been redshifted to lower energies. A redshift $z \sim 20$ would be required to produce the low observed $E_{\text{pk}}^{\text{obs}}$ value. This is clearly at odds with the redshift constraint just determined and also with the redshift constraint derived from the optical data.

Using the redshift constraint derived assuming the Amati et al. (2002) relation, we can compare the rest-frame X-ray afterglow and burst luminosities with values found for GRBs. It is interesting to note that the E_{iso} we derive for the burst is approximately the “standard energy” found for GRBs by Frail et al. (2001). This would appear to indicate that XRF 030723 was an approximately spherical (i.e. non-jetted) explosion, with an energy release typical of core-collapse supernovae. However, the light curve break at $t \sim 1.5$ days (Section 3) argues very strongly for jetted emission. Moreover, the afterglow energetics suggest further problems with this simple picture. Similar to the tight clustering of burst energies found by Frail et al. (2001), Berger, Kulkarni, & Frail (2003) find that the isotropic equivalent emission in the X-ray afterglow (at 10 hours after the GRB) also becomes tightly clustered if one accounts for differences in the jet half-opening angles $\Delta\theta$. As displayed in Figure 9, we find that XRF 030723 extends the Berger, Kulkarni, & Frail (2003) correlation to much lower luminosities. In the case of XRF 030723, the simple flat-top jet picture would imply $\Delta\theta > \pi$, which violates the model for both the burst and afterglow. This appears to be the case for GRB 031203 (see, Watson et al. 2004; Sazanov, Lutovinov, & Sunyaev 2004) as well. The E_{iso} values for these under-energetic bursts (including also XRF 020903) are

less than the minimum energies permitted in the simple model where GRBs and XRFs have a standard energy release, with the observed energy determined by the width of the flat-top GRB jet. This is also the case for GRB 980425, if the association with SN 1998bw is correct (Kouveliotou et al. 2004).

We can seek to retain a unified picture for GRBs and XRFs by modifying the energetics of the explosion, as in the dirty fireball (Dermer, Chiang, & Böttcher 1999; Huang, Dai, & Lu 2002) or clean fireball (Mochkovitch et al. 2003) models, and/or by adopting a more complex description of the jet. In Section 3 we summarize extensions of the simple one component, on-axis, flat-top jet picture, which were found necessary to account for the complex behavior of the XRF 030723 optical afterglow. In particular, several authors suggest the possibility of a jet viewed off-axis. We can estimate that $E_{\text{pk}}^{\text{obs}}$ would decrease by a factor $\delta = 1 + \gamma^2(\theta_v - \Delta\theta)^2$ (see, e.g., Yamazaki et al. 2002) if the jet with Lorentz factor γ were viewed at angle θ_v from its center. A typical GRB would have $E_{\text{pk}}^{\text{obs}} \sim 200$ keV and $\gamma \sim 150$. Our measured $E_{\text{pk}}^{\text{obs}}$ then implies $\theta_v - \Delta\theta \approx 1.8$ degrees. The on-axis E_{iso} would scale up by factor $\sim \delta^3$ to $E_{\text{iso}} \sim 2 \times 10^{54}$ erg, which is similar to values calculated for classical GRBs. At early times, a burst and afterglow viewed in such fashion would exhibit a flat or possibly rising light curve due to the competing effects of the fading afterglow flux and the jet expanding into the line of sight. At late times, the flux would break and decay as t^{-2} , which is the canonical late time decay law observed for GRBs. For a typical GRB circumburst density of 1 cm^{-3} , and using the formulas of Sari, Piran, & Halpern (1999), the break would occur at $t \sim 1.5$ days—as observed for the optical light curve (and possibly X-ray light curve; Section 5.3) of XRF 030723—if $\Delta\theta \sim 4$ degrees. Hence, off-axis jets can explain the complex behavior of the optical afterglow flux. Huang et al. (2004) also argue for off-axis viewing. In their model, a narrow jet with parameters similar to those above leads to the afterglow rebrightening at $t \gtrsim 9$ days (see below and Section 3). The early-time afterglow light curve is due to an additional wide ($\Delta\theta \sim 17$ degree), baryon-loaded ($\gamma \sim 30$), and off-axis ($\theta_v \sim 21$ degrees) jet.

One important caveat is that the on-axis event would be a $\sim 3\sigma$ outlier on the Amati et al. (2002) plot. Therefore, off-axis jetting implies that XRFs should be sub-energetic outliers on the relation (see also, Figure 2 of Yamazaki, Kunihiro, & Nakamura 2004). This may be the case for XRF 030723 if the redshift is ~ 0.1 (Figure 8). Ghirlanda, Ghisellini, & Lazzati (2004) have recently discovered a correlation between E_γ —the beaming corrected prompt energy release—and $E_{\text{pk}}^{3/2}$, which appears to be tighter than the $E_{\text{iso}} \propto E_{\text{pk}}^2$ correlation. If we ignore the off-axis possibility and follow Ghirlanda, Ghisellini, & Lazzati (2004) in calculating $E_\gamma = (1 - \cos \Delta\theta) \cdot E_{\text{iso}} \sim 3 \times 10^{48}$ erg, we likewise find that XRF 030723 satisfies the correlation. Here we use $\Delta\theta = 10$ degrees, because the observed burst flux requires a broader jet in order to get the afterglow to break at $t \sim 1.5$ days. If we consider the case

where the off-axis GRB discussed above is viewed on axis, we find $E_\gamma(\propto E_{\text{iso}}^{3/4}) \sim 5 \times 10^{51}$ erg. The on-axis event is a $\sim 4\sigma$ outlier. Future prompt XRF observations will be critical to determine the scatter in the correlations and to determine whether or not XRFs demand a more complex jet model.

5.3. X-ray Afterglow Rebrightening?

Given the apparent slow X-ray afterglow fade between our E1 and E2 *Chandra* observations (possibly $\propto t^{-1}$, Section 4.2), the afterglow spectrum is consistent with a smooth extrapolation of the XRF spectrum (in spectral shape and marginally in spectral flux (see Figure 7)) from $t \sim 30$ s. These facts suggest a simple evolution, where the X-ray afterglow has not undergone a temporal break prior to $t \sim 13$ days. A very similar argument is made by Amati et al. (2004) for XRF 020427 based on data from *BeppoSAX*. Contrarily, we have evidence for complex temporal behavior in the optical afterglow of XRF 030723, which was not available for for XRF 020427. It is possible that the slow fade indicated by the ratio of our E1 and E2 *Chandra* fluxes was produced by a more complex, time-varying flux—possibly a rapid ($\propto t^{-2}$) fade followed by a rebrightening ($\propto t^{3.5}$) as observed in the optical.

To test whether an X-ray rebrightening is or is not present in the *Chandra* data, we examine the arrival times and energies of each source count in our E1 and E2 observations. These data are expected to provide further constraining information than would be provided by the integrated fluxes alone. We seek the model which maximizes the likelihood:

$$\mathcal{L}(t_1, t_2, \dots, t_n, E_1, E_2, \dots, E_n) = r(t_1, E_1) \cdot r(t_2, E_2) \cdot \dots \cdot r(t_n, E_n) \cdot \exp \left\{ - \int_{E_0}^{E_f} \int_{t_0}^{t_f} r(t', E') dt' dE' \right\},$$

where the rate $r(t, E)$ is evaluated for each of n observed events, and where the time integral in the exponential is carried out for the good time intervals of *Chandra* data acquisition. We consider the data in the 0.5-8.0 keV band. Assuming that the spectral slope does not evolve with time, we write the the event rate as $r(t, E) = c(E) * \phi(t)$, where $c(E)$ is the best fit count rate model from Section 4.2 (see also Figure 6), and $\phi(t)$ is the time-dependent normalization. For $\phi(t)$ we use a broken power-law:

$$\phi(t) = \begin{cases} \phi_0 \left(\frac{t}{t_b} \right)^{\alpha_1}, & \text{if } t \leq t_b \\ \phi_0 \left(\frac{t}{t_b} \right)^{\alpha_2}, & \text{if } t > t_b, \end{cases} \quad (1)$$

with $t_b = 9$ days, as suggested by the optical decay curve. The source data are extracted from 2.83'' and 0.84'' radius regions, respectively, for E1 and E2. This yields 76 and 74

events, respectively, for E1 and E2. We ignore the effect of the ~ 1 background event in each epoch.

Fitting first for the case $\alpha_1 = \alpha_2 = \alpha$ (i.e. no break), we find $\alpha = -0.9_{-0.2}^{+0.1}$, in agreement with the index determined above. Next, we allow the indices to vary independently. We find $\alpha_1 = -2.1_{-2.5}^{+2.0}$ and $\alpha_2 = 3.5_{-7.4}^{+8.7}$. These best-fit values are quite similar to their respective values measured from the optical data. Comparing the likelihood calculated for each of these models, we have $-2\Delta \log(\mathcal{L}) = 1.08$. This quantity is expected to be approximately χ^2 distributed with one degree of freedom. Hence, the rebrightening model is preferred by the data at approximately 70% confidence. We determine a similar estimate (68% confidence that the normalized event rate versus fraction of time observed is different in E1 from that in E2) from a KS-test of the photon arrival time distributions, ignoring the photon energies. This estimate does not require an event rate model.

5.4. The Nature of the Rebrightening

In Section 5.3, we discuss marginal evidence that the X-ray afterglow flux tracks the optical afterglow flux. We know of one case where a rebrightening in the X-ray afterglow was tracked by the optical afterglow: GRB 970508, with a rebrightening at $t \sim 1$ day (Piro et al. 1998). Because it is also common for broad-band fades as t^{-2} to occur at late times, we regard a slow X-ray fade accompanying a considerably more rapid optical fade after 1.5 days as unlikely. If a slow fade were present in the optical and not in the X-rays, we would expect to see an evolution in the spectral flux between the optical and X-ray bands. However, the afterglow spectrum in the optical (see, Fynbo et al. 2004a) and in the X-rays is consistent with a power-law spectrum with photon index $\Gamma = 2$, and this spectral slope does not appear to evolve (in the X-rays or in the optical) between our E1 and E2 *Chandra* observations. If we fit the optical flux model (Figure 7) to the *Chandra* count rates in E1 and E2, then the spectral slope (photon index) connecting the two bands is found to be $\Gamma = 2.0 \pm 0.1$, consistent with the slopes in the optical and X-ray data considered alone. Within the context of the standard fireball shock model, this broad-band slope suggests a slow-cooling synchrotron spectrum where the cooling break frequency is below the optical band (see, e.g., Sari, Piran, & Narayan 1998).

Alternatively, it may be that the X-ray fade at $t \gtrsim 1.5$ days is in fact slower than the optical fade due to the onset of an inverse-Compton (IC) emission component (see, e.g., Figure 3 of Panaitescu & Kumar 2000). This would require a fairly dense circumburst medium with $n \sim 100 \text{ cm}^{-3}$. We would also expect to observe a flattening out of the E2 spectrum relative to E1 by $\Delta\Gamma \geq 0.5$ (Sari & Esin 2001). However, such a flattening is

excluded by the *Chandra* data at 97.6% confidence ($\Delta\chi^2 = 5.1$ for 1 additional degree of freedom).

If the same mechanism is responsible for the rebrightening at $t \gtrsim 9$ days in both the optical and in the X-ray bands, then an explanation in terms of a supernova bump is incorrect. If the bump were produced by a dust echo, we might expect to have observed a softening of the X-ray spectrum in E2, as was observed for the possible dust echo in GRB 031203 by Vaughan et al. (2004). Another possibility is that the afterglow shock interacts with a density enhancement. Lazzati et al. (2002) find that the afterglow spectrum beyond the synchrotron cooling break is insensitive to density enhancements. However, the more complex Wolf-Rayet wind models of Ramirez-Ruiz et al. (2001) are capable of producing significant late time bumps (see their Figure 5). Ramirez-Ruiz et al. (2001) also suggest the possibility that a dense shell of material from a progenitor wind could generate a bump as a Compton echo of the prompt emission (see their Figure 6). Shortward of the hard X-rays, this bump would have a spectrum mirroring that of the prompt emission, as we seem to observe. This scenario requires off-axis viewing for the bump to be a substantial contributor to the afterglow flux. Also in the off-axis picture, the two-component jet model of Huang et al. (2004) would produce a rise in the X-rays as well as in the optical.

In the context of a supernova bump, Fynbo et al. (2004a) explain the spectral reddening at $t \approx 27$ days (i.e. after the bump) as due to UV line-blanketing. Alternatively, reddening could change as function of time if the progenitor has a complex mass loss history, including a Wolf-Rayet phase and a dusty wind (see, e.g., Mirabal et al. 2003; Ramirez-Ruiz et al. 2001).

6. Conclusions

We have determined the temporal and spectral properties of XRF 030723, as detected and measured by the WXM and FREGATE instruments on *HETE-2*. The duration of the burst is similar to that common in long-duration GRBs. Moreover, the burst spectral properties are similar to those of GRBs detected by FREGATE, except that the burst peak energy $E_{\text{pk}}^{\text{obs}}$ is ~ 10 keV rather than ~ 200 keV. The low burst fluence appears to be consistent with an extension of the Amati et al. (2002) relation to XRFs. We have derived power-law spectral parameters to the X-ray afterglow data taken in two epochs with *Chandra*. The photon index we derive is a typical value for long-duration GRBs, further strengthening the link between XRFs and long-duration GRBs. We have argued that the X-ray data, particularly when compared to the optical afterglow data, favor a complex jet structure and off-axis viewing, possibly also a complex circumburst medium due to a progenitor wind.

We wish to stress the importance of multi-band observations, including X-ray observations, to separate out and quantify these effects. We encourage further late time ($t \gtrsim 1$ week) observations with *Chandra* and/or *XMM-Newton* to help determine the nature of possible rebrightenings in future afterglow light curves.

We thank Harvey Tananbaum for his generous allocation of Director’s Discretion Time for the *Chandra* observations. This research was supported in part by NASA contract NASW-4690.

REFERENCES

- Amati, L., et al. 2002, A&A, 390, 81
- Amati, L., et al. 2004, A&A, 426, 415
- Atteia, J.-L. 2003, A&A, 407, L1
- Band, D. L., et al. 1993, ApJ, 413, 281
- Barraud, C., et al. 2003, A&A, 400, 1021
- Bloom, J. S., Frail, D. A., & Kulkarni, S. R. 2003, ApJ, 594, 674
- Berger, E., et al. 2003, Nature, 426, 154B
- Berger, E., Kulkarni, S. R., & Frail, D. A. 2003, ApJ, 590, 379
- Bond, H. E. 2003, GCN, 2329
- Butler, N., et al. 2003a, GCN, 2328
- Butler, N., et al. 2003b, GCN, 2347
- Costa, E., et al. 1999, A&AS, 138, 425
- Dado, S., Dar, A., & De Rujula, A. 2003, astro-ph/0309294
- Dermer, C. D., Chiang, J., & Böttcher, M. 1999, ApJ, 513, 656
- Dickey & Lockman 1990 ARAA, 28, 215
- Dullighan, A., et al. 2003a, GCN2326

- Dullighan, A., et al. 2003b, GCN, 2336
- Fox, D. B., et al. 2003, GCN, 2323
- Frail, D. A., et al. 2001, ApJ, 562, L55
- Fynbo, J. P. U., et al. 2004a, ApJ, 609, 962
- Fynbo, J. P. U., et al. 2004b, astro-ph/0402264
- Ghirlanda, G., Ghisellini, G., & Lazzati, D. 2004, astro-ph/0405602
- Henden, A. 2003, GCN, 2343
- Heise, J., et al. 2000, in Proc. 2nd Rome Workshop: Gamma-ray Bursts in the Afterglow Era, eds. E. Costa, F. Frontera, J. Hjorth (Berlin: Springer-Verlag), 16
- Huang, Y. F., Dai, Z. G. & Lu, T. 2002, MNRAS, 332, 735
- Huang, Y. F., et al. 2004, ApJ, 605, 300
- Kawai, N., et al. 2003, GCN, 2412
- Kippen, R. M., et al. 2002, in Gamma-ray Bursts and Afterglow Astronomy, eds. G. R. Ricker and R. Vanderspek (New York: AIP), 244
- Kouveliotou, C., et al. 2004, ApJ, 608, 872
- Lazzati, D., et al. 2002, A&A, 396, 5
- Lewin, W. H. G., van Paradijs, J. & Taam, R. E. 1993, Space Sci. Rev., 62, 223
- Liang, E. W., & Dai, Z. G. 2004, ApJ, 608, L9
- Mirabal, N., et al. 2003, ApJ, 595, 935
- Mochkovitch, R., et al. 2004, in Proc. 3rd Rome Workshop: Gamma-ray Bursts in the Afterglow Era, eds. M. Feroci, F. Frontera, N. Masetti, L. Piro (San Francisco: ASP), 381
- Panaitescu, A., & Kumar, P. 2000, ApJ, 543, 66
- Piro, L., et al. 1998, A&A, 331, L41
- Prigozhin, G., et al. 2003, GCN, 2313

- Ramirez-Ruiz, E., et al. 2001, MNRAS, 327, 829
- Rosati, P., et al. 2002, ApJ, 566, 667
- Rykoff, E. S., et al. 2003, ApJ, 601, 1013
- Sakamoto, T., et al. 2003, ApJ, 602, 875
- Sari, R., Piran, T., & Narayan, R. 1998, ApJ, 497, L17
- Sari, R., Piran, T., & Halpern, J. P. 1999, ApJ, 519, L17
- Sari, R., & Esin, A. A. 2001, ApJ, 548, 787
- Sazonov, S. Yu., Lutovinov, A. A., & Sunyaev, R., A. 2004, Nature, 430, 646
- Schlegel, D., et al. 1998, ApJ, 500, 525
- Shirasaki, Y., et al. 2000, SPIE, 4012, 166
- Shirasaki, Y., et al. 2003, SPIE, 4851, 1310.
- Smith, D. A., et al. 2003, GCN, 2338
- Soderberg, A. M., Berger, E., & Frail, D. A. 2003, GCN, 2330
- Soderberg, A. M., et al. 2004, ApJ, 606, 994
- Soderberg, A. M., et al. 2004, Nature, 430, 648
- Strohmayer, T. E., et al. 1998, ApJ, 500, 873
- Tominaga, N., et al. 2004, ApJ, 612, L105
- Vaughan, S., et al. 2004, ApJ, 603, L5
- Watson, D., et al. 2004, astro-ph/0401225
- Woosley, S. 2004, Nature, 430, 623
- Yamazaki, R., Ioka, K., & Nakamura, T. 2002, ApJ, 571, L31
- Yamazaki, R., Kunihiro, I., & Nakamura, T. 2004, ApJ, 606, L33
- Zhang, B., & Mészáros, P. 2002, ApJ, 581, 1236

Table 1: Temporal properties of XRF 030723.

Energy Band (keV)	Counts (in ~ 35 s)	Rate _{peak} (1/s)	t ₅₀ (s)	t ₉₀ (s)
2 - 5	624	43.3	11.3 \pm 1.3	24.1 \pm 3.5
5 - 10	530	34.8	14.4 \pm 3.6	32.5 \pm 3.0
10 - 25	357	40.3	13.6 \pm 4.0	29.8 \pm 5.8
2 - 25	1430	81.2	12.0 \pm 1.3	28.3 \pm 2.5

Note.—The quoted errors correspond to $\pm 1\sigma$. Burst counts and rates in the WXM are determined by subtracting a linear (in time) background model (horizontal dotted lines in Figure 2).

Table 2. Results of fits to the WXM+FREGATE spectrum of XRF 030723.

Model	kT (keV)	α	β	$E_{\text{peak}}^{\text{obs}}$ (keV)	Norm.	χ^2_{ν} (DOF)
blackbody	2.0 $^{+0.5}_{-0.4}$				8.6 \pm 1.5 $\times 10^{-2}$	1.065 (82)
power-law			-2.0 \pm 0.2		2.1 \pm 0.3	0.835 (82)
cutoff power-law		-1.0 (fixed)		9.3 $^{+3.6}_{-2.5}$	0.8 $^{+0.3}_{-0.2}$	0.809 (82)
Band		-1.0 (fixed)	-3.4 $^{+1.0}_{-...*}$	9.4 $^{+2.0}_{-1.6}$	8.0 $^{+1.3}_{-1.2}$ $\times 10^{-3}$	0.816 (81)
Band		-1.4 \pm 0.4	-3.0 $^{+0.8}_{-...*}$	9.7 $^{+6.0}_{-2.5}$	2.0 $^{+7.4}_{-1.5}$ $\times 10^{-3}$	0.816 (80)

Note.—The quoted errors correspond to the 90% confidence region, except for the Band models, where errors are 68% confidence.

* The data do not allow for a determination of the lower limits for the Band model β parameter.

Table 3: Peak photon number and energy fluxes (in 1 s) and fluences in various energy bands for XRF 030723.

	2-30 keV	30-400 keV	2-400 keV
Peak flux (ph cm $^{-2}$ s $^{-1}$)	2.0 $^{+0.4}_{-0.3}$	0.1 \pm 0.1	2.1 \pm 0.4
Peak flux (10 $^{-8}$ ergs cm $^{-2}$ s $^{-1}$)	2.6 \pm 0.5	0.9 $^{+1.8}_{-0.7}$	3.5 $^{+1.8}_{-1.1}$
Fluence (10 $^{-7}$ ergs cm $^{-2}$)	2.9 \pm 0.5	0.2 $^{+0.3}_{-0.1}$	3.0 $^{+0.7}_{-0.6}$

Note.—All of the quantities in this table are derived assuming a cutoff power-law model with $\alpha = -1$ for the spectrum. The quoted errors correspond to the 90% confidence region.

Table 4: Characteristics of the three *Chandra* sources detected within the SXC error region.

#	Chandra Name	E1 Cts (bg)	E2 Cts (bg)
1	CXOU J214924.4-274248	78.5 (1.5)	75.6 (2.4)
3	CXOU J214926.9-274146	19.9 (3.1)	121.8 (4.2)
4	CXOU J214928.7-274211	16.2 (3.8)	98.1 (4.9)

Note.—We estimate a position uncertainty of $1.4''$. A steady source would have an E2 count rate ~ 6 times greater than the E1 count rate.

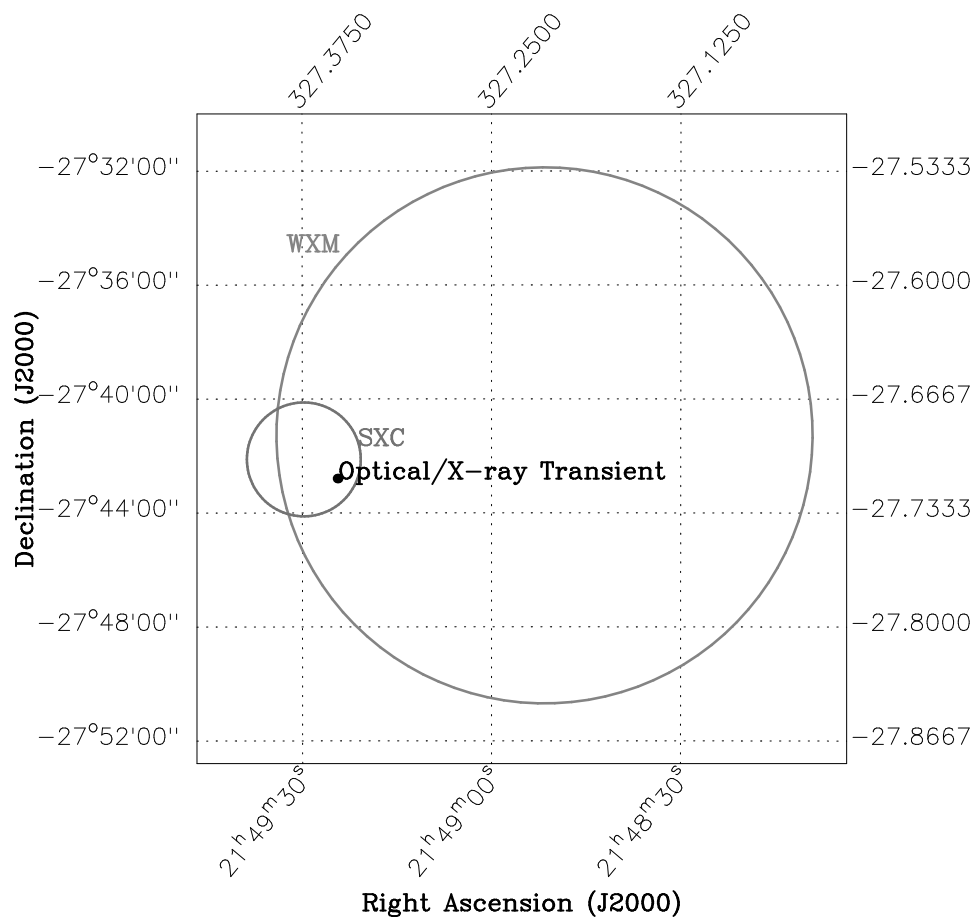


Fig. 1.— *HETE-2* WXM/SXC localization for XRF 030723. The larger circle is the 90% confidence WXM error region, and the smaller circle is the SXC 90% confidence error region (Prigozhin et al. 2003). The final *HETE-2* error region is the SXC error region. The point labeled “Optical/X-ray Transient” refers to the location of the spatially coincident optical and X-ray afterglows to XRF 030723 reported by Fox et al. (2003) and by Butler et al. (2003b), respectively.

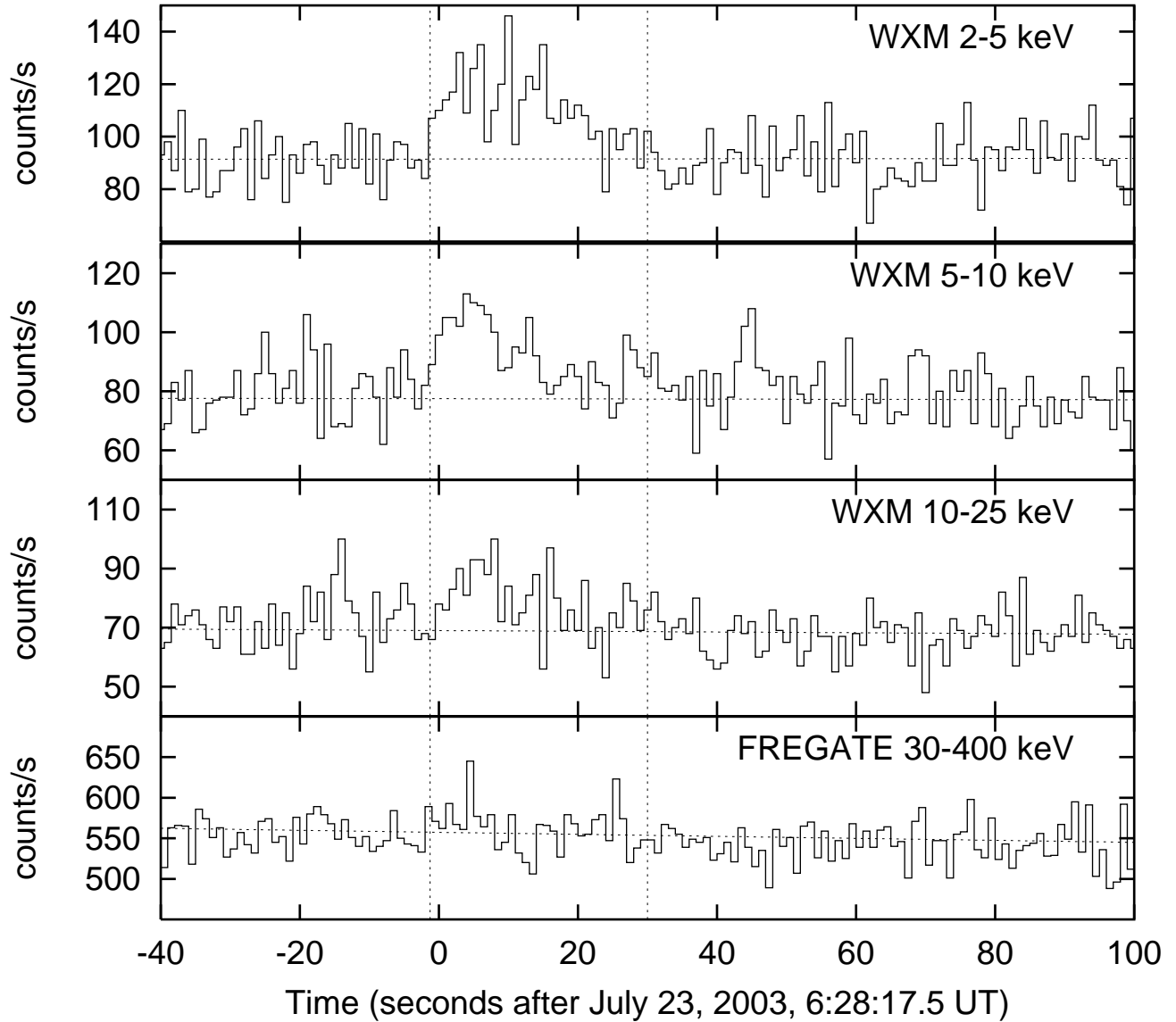


Fig. 2.— Light curve for XRF 030723 in three WXM energy bands (2-5 keV, 5-10 keV, 10-25 keV) and for FREGATE in the 30-400 keV band. The data are binned in one second intervals. Source data for spectral fitting are extracted from the region between the vertical dotted lines (between -1.25 and 30 seconds). The background fits are plotted as horizontal dotted lines.

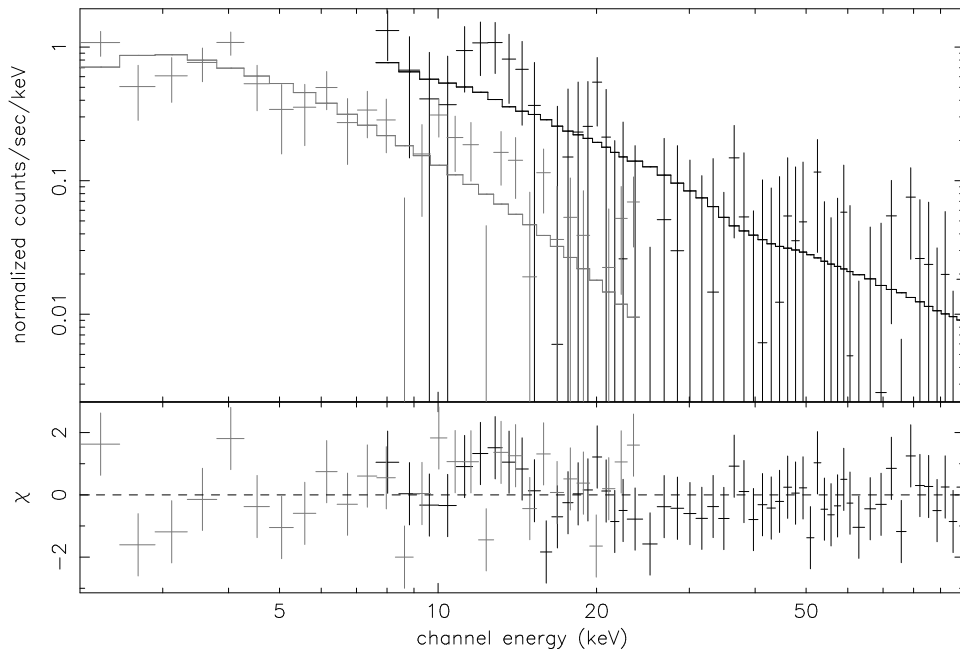


Fig. 3.— WXM and FREGATE spectra for XRF 030723. Data are fitted jointly for the WXM (2-25 keV) and FREGATE (7-100 keV) from the time interval -1.25 to 30 seconds. The model shown as histograms plotted with the data (crosses) is the best-fit power-law model (Table 2).

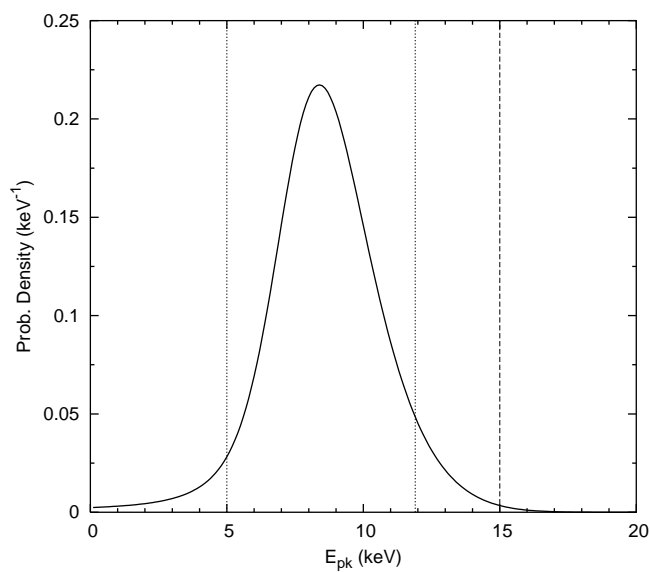


Fig. 4.— The posterior probability density distribution for $E_{\text{pk}}^{\text{obs}}$ from the constrained Band model. This is calculated by numerically integrating $\exp(-\chi^2/2)$ over the constrained Band model normalization and β parameters, then normalizing the resulting $E_{\text{pk}}^{\text{obs}}$ distribution. The vertical dotted lines define the 90% probability interval, and the vertical dashed line defines the 99.7% probability upper limit of 15 keV. The peak of the probability occurs at $E_{\text{pk}}^{\text{obs}} = 8.4$ keV.

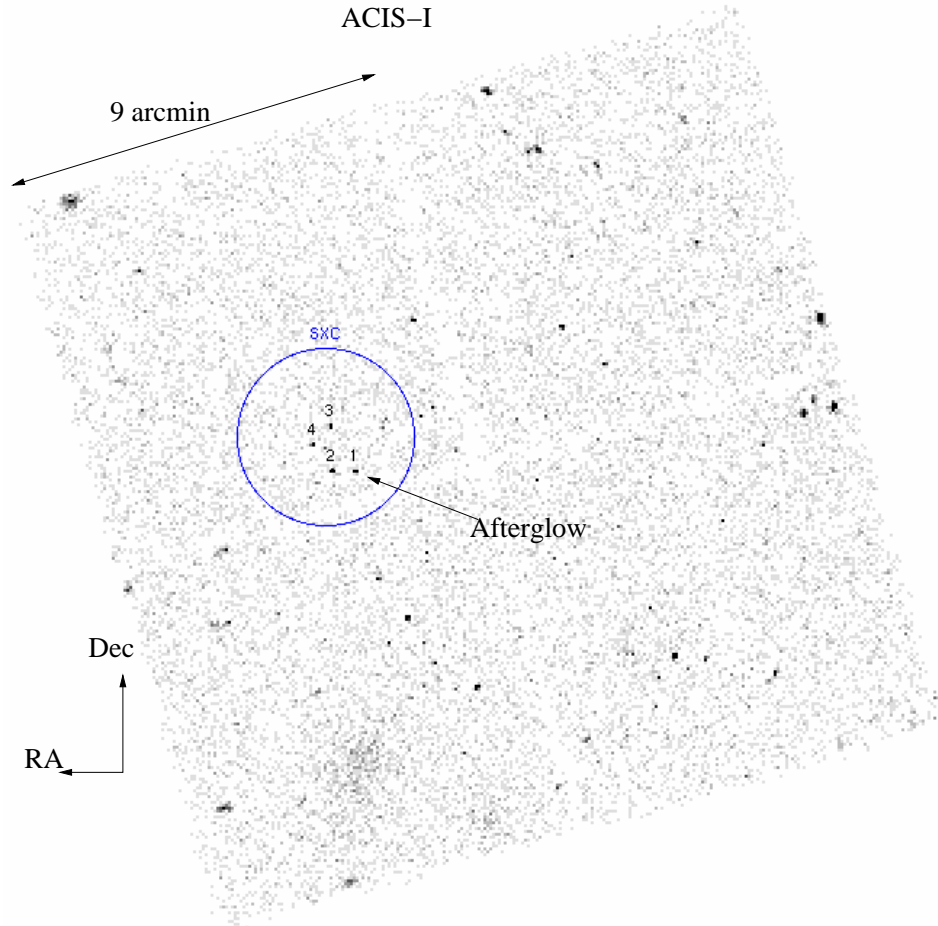


Fig. 5.— Three X-ray sources and one USNO field star (source #2) were found within the SXC error region in our E1 ACIS-I observation. The brightest source #1, spatially coincident with a source later confirmed by Fox et al. (2003), is labelled “Afterglow.” Our E2 observation with ACIS-S3 revealed that this source faded in the X-ray’s as well.

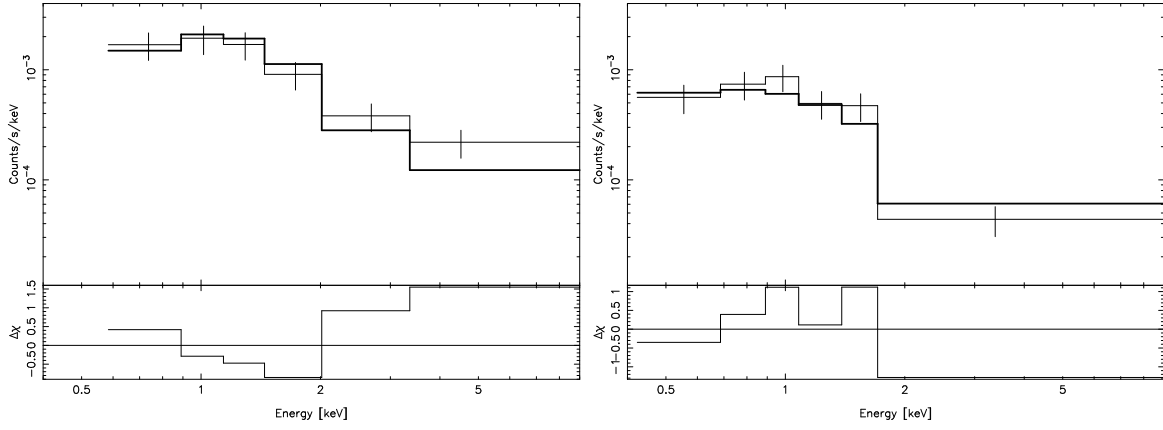


Fig. 6.— The counts in E1 (ACIS-I, left plot) and E2 (ACIS-S, right plot) are fitted simultaneously using an absorbed power-law model ($\chi^2_{\nu} = 8.9/9$).

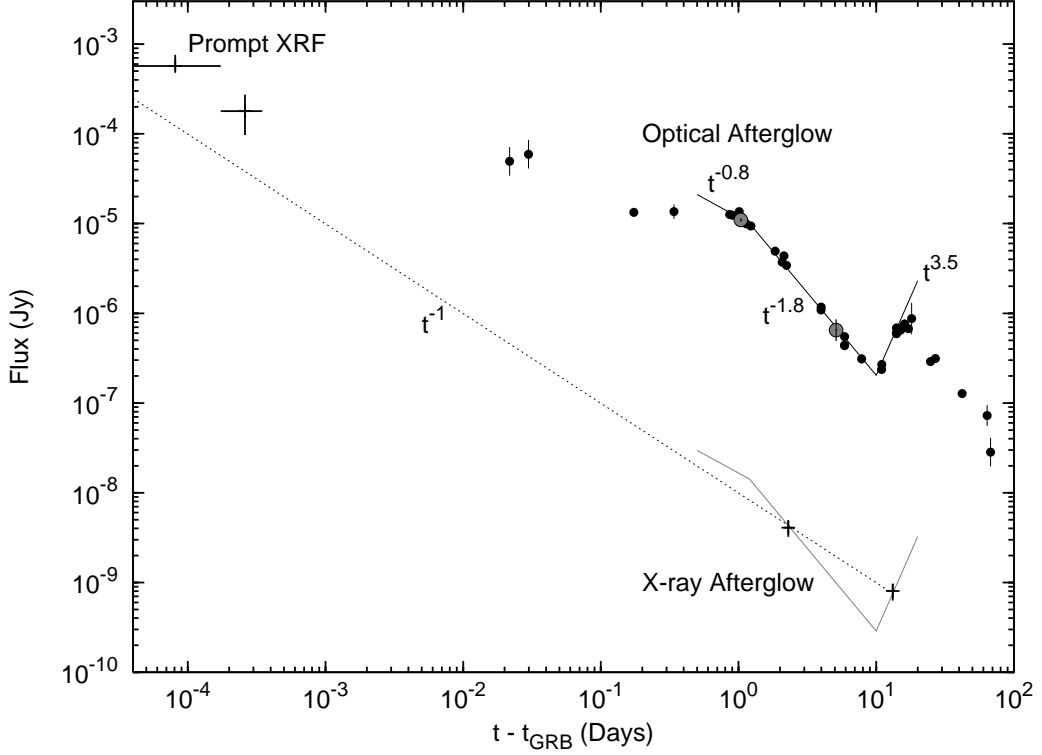


Fig. 7.— The optical spectral flux and the X-ray spectral flux (at 1 keV) for the afterglow to XRF 030723. The optical data are taken from the literature (Fox et al. 2003; Dullighan et al. 2003a,b; Bond 2003; Smith et al. 2003; Fynbo et al. 2004a). Our data are marked with open circles. All optical data are from the R-band, except for the left-most two points from (Smith et al. 2003), which are unfiltered. We apply an extinction correction to the optical data of 0.088 mag (Schlegel et al. 1998). A temporal break appears to be present in the spectrum at $t \sim 1.5$ days (Dullighan et al. 2003b). A rebrightening is present after $t \sim 9$ days (Fynbo et al. 2004a). We overplot a 3-times broken power-law fit, to describe the optical behavior. The X-ray afterglow spectral flux may follow this same trend (gray line), or the behavior may be that of a simple power-law fade (dotted line).

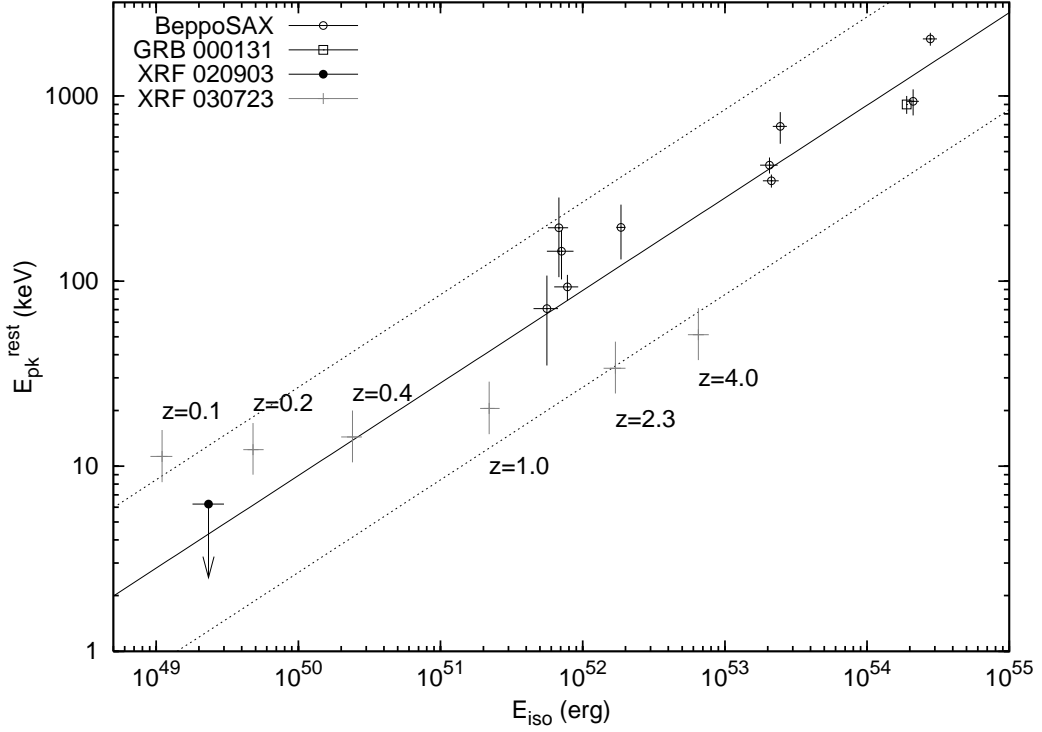


Fig. 8.— The trajectory with redshift of XRF 030723 through the $E_{\text{pk}}-E_{\text{iso}}$ plane (crosses), where E_{iso} is the isotropic-equivalent radiated energy between $1-10^4$ keV and E_{pk} is the peak of the νF_{ν} spectrum, both measured in the rest frame of the burst. The solid line is given by the equation $E_{\text{pk}} = 89(E_{\text{iso}}/10^{52}\text{erg})^{0.5}$ keV. The dotted region around this curve represents the 90% confidence region, where we describe the intrinsic scatter in the Amati et al. (2002) relation as lognormal, with standard deviation 0.3. The filled circle in the lower left-hand corner is the location of XRF 020903. The ten open circles are the *BeppoSAX* GRBs reported by Amati et al. (2002). Given the constraint from the optical that $z < 2.3$, the XRF 030723 data (like the XRF 020903 data) are consistent with an extension of the Amati et al. (2002) relation to XRFs.

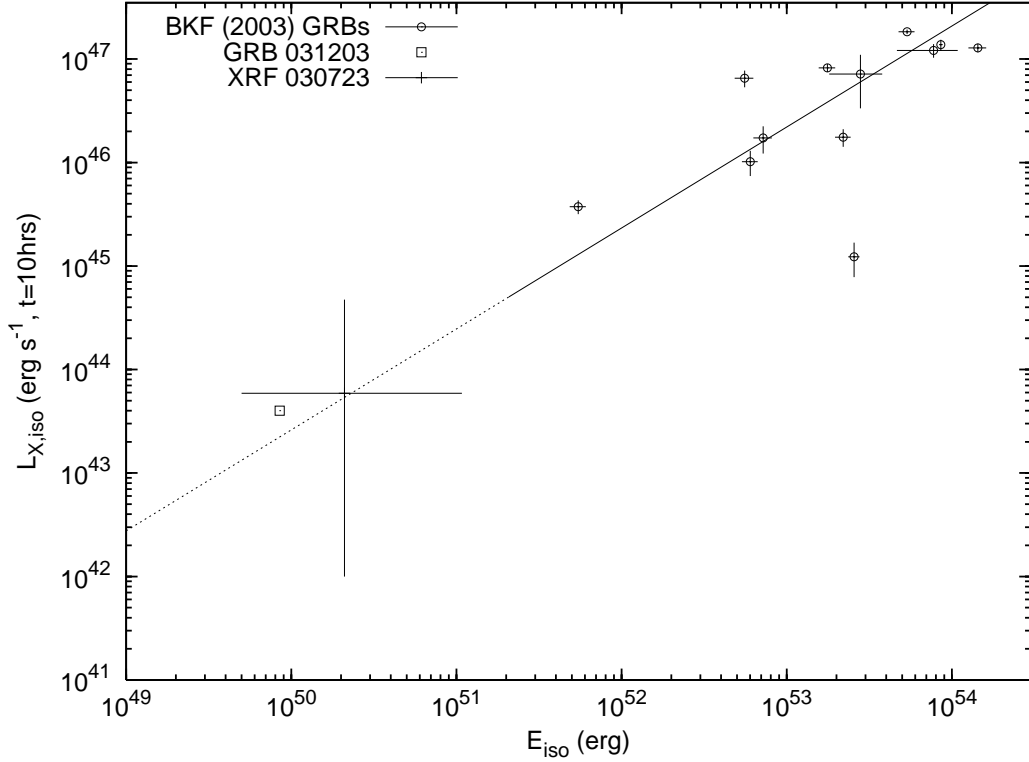


Fig. 9.— The location of XRF 030723 in the $L_{X,\text{iso}} - E_{\text{iso}}$ plane, where $L_{X,\text{iso}}$ is the isotropic-equivalent luminosity in the 2-10 keV band, adjusted to $t = 10$ hrs after the burst, measured in the rest frame of the burst. For XRF 030723, we include the errors in the X-ray flux, temporal index ($\alpha = -1.0 \pm 0.1$), and redshift. The XRF 030723 data extend a correlation found by Berger, Kulkarni, & Frail (2003) for GRBs. E_{iso} values for the Berger, Kulkarni, & Frail (2003) GRBs were taken from Bloom, Frail, & Kulkarni (2003). Following Kouveliotou et al. (2004), we also plot the value for the *INTEGRAL* burst GRB 031203. The solid line represent the best fit linear regression of Berger, Kulkarni, & Frail (2003), based on a flat-top, single-component jet model. We extend this line to jet opening angles $\theta_{\text{jet}} > \pi$ (dotted region).